Multiple twinning in pure hexagonal close-packed titanium

Lei Bao, Yudong Zhang, Christophe Schuman, Jean-Sébastien Lecomte, Marie-Jeanne Philippe, Xiang Zhao, Claude Esling

Journal of
Applied Crystallography

ISSN 0021-8898

Received 5 March 2013
Accepted 10 August 2013

Multiple twinning in pure hexagonal close-packed titanium

Lei Bao,[a,b] Yudong Zhang,[b,c] Christophe Schuman,[b] Jean-Sébastien Lecomte,[b] Marie-Jeanne Philippe,[b] Xiang Zhao[d] and Claude Esling[b,c]*

[a]Key Laboratory of the Electromagnetic Processing of Materials of the Ministry of Education, Northeastern University, Shenyang 110819, People's Republic of China, [b]Laboratoire d'Étude des Microstructures et de Mécanique des Matériaux, LEM3, CNRS UMR 7239, Université de Lorraine, 57045 Metz, France, [c]Laboratoire d'Excellence 'DAMAS' (Design of Metal Alloys for Low-Mass Structures), Université de Lorraine, 57045 Metz, France, and [d]Key Laboratory for Anisotropy and Texture of Materials of the Ministry of Education, Northeastern University, Shenyang 110819, People's Republic of China. Correspondence e-mail: claude.esling@univ-lorraine.fr

Commercial pure titanium (T40) was deformed in channel die compression by means of the split-sample technique in order to study multiple twinning. Particular attention was paid to the twin variant presentation and selection during multiple twinning. All possible misorientations, corresponding to the multiple twins arising from the combination of the $\{11\bar{2}2\}$ compression (C) twin, the $\{10\bar{1}2\}$ tension twin (T1) and the $\{11\bar{2}1\}$ tension twin (T2), were calculated with respect to the crystal basis of the matrix grain. All the multiple twin variants are partitioned into ten classes with the same crystallographically equivalent misorientation angle and axis. However, when the influence of twinning order is taken into account, the multiple twin variants are partitioned into 15 classes. Experimental results prove that the selection of twin variants (primary and secondary) is mainly governed by their macroscopic Schmid factor (SF). The normalized SF is more efficient at predicting variant selection. A twin formed in one grain can activate another twin in a neighbouring grain, provided that the angle between the two twinning planes does not exceed 20°.

1. Introduction

Mechanical twinning is a particularly important deformation mode in α-titanium (Vedoya *et al.*, 1988; Philippe *et al.*, 1995; Fundenberger *et al.*, 1997; Zaefferer, 2003). It is an important factor in the control of the properties of titanium such as ductility and fracture strength (Kocks & Westlake, 1967; Partridge, 1967; Mahajan & Williams, 1973; Yoo, 1981). Many studies have been carried out on mechanical twinning and texture in titanium and other metals (Bevis & Tomsett, 1970; Cheneau-Späth *et al.*, 1994; Balogh *et al.*, 2009), as well as on the well established Dauphiné twin in quartz crystals (Chateigner *et al.*, 2002). Twins can be described by elegant methods in mathematical crystallography (*e.g.* Nespolo & Ferraris, 2000, 2003, 2004, 2006; Nespolo, 2004). Several authors of this paper have also applied mathematical methods imported from number theory, notably Bezout's theorem (Zhang *et al.*, 2010), to develop a general method to determine twinning elements. The purpose of the present paper is to study mechanical twinning in α titanium, which belongs to the space group $P6_3/mmc$, with cell parameters $a = b = 2.9508$ Å, $c = 4.6855$ Å, $c/a = 1.58787$, $\alpha = \beta = 90°$ and $\gamma = 120°$. Indeed, when polycrystalline titanium is deformed plastically, twinning is one of the possible mechanisms to adapt the plastic deformation, together with dislocation slip. At room temperature, three major twin systems are commonly observed in α titanium: the $\{10\bar{1}2\}$, $\{11\bar{2}1\}$ and $\{11\bar{2}2\}$ twin systems (Philippe *et al.*, 1988). The $\{10\bar{1}2\}$ and $\{11\bar{2}1\}$ systems are referred to as tension twins and $\{11\bar{2}2\}$ as a compression twin, because they are activated under tension or compression load along the c axis of the parent crystal (Rosi *et al.*, 1956). Once a twin forms, it leads to a change in orientation of the twin with respect to the parent crystal by a certain rotation depending on the twinning system. The new orientation may be in a favourable orientation for a new twinning (secondary twinning, for example). A secondary twin inside an existing primary twin is called a double twin (Barnett *et al.*, 2008; Martin *et al.*, 2010). In titanium, double twins formed from the combination of the $\{10\bar{1}2\}$ tension twin (T1) and the $\{11\bar{2}2\}$ compression twin (C) are commonly observed in rolling and compression deformation (Bao, Schuman *et al.*, 2010). At present, it is well accepted that variant selection for primary twins follows Schmid's law (Lebensohn & Tome, 1993), which means that those variants with the highest resolved shear stress have a higher probability of being activated. In extruded magnesium alloy tubes, it is also found that the active twins correspond to those possessing high values of the Schmid factor (SF) (Godet *et al.*, 2006). However, in the case of secondary twinning, Barnett *et al.* (2008) reported that variant selection does not follow

Schmid's law. Jonas and co-workers (Jonas *et al.*, 2011; Martin *et al.*, 2010) concluded that, in a magnesium alloy, Schmid's law is not the only factor affecting variant selection, and common volumes and primary-to-secondary accommodation shears would play more important roles. Recently, Mu *et al.* (2012) systematically studied variant selection in primary, secondary and tertiary twins in magnesium alloys, and found that the primary twin selected is not necessarily the variant with the highest Schmid factor but the one that requires the least accommodation work in most of the neighbouring grains. The same principle was found to hold for the secondary and tertiary twins as well.

For titanium, although it possesses a hexagonal close-packed (h.c.p.) structure, the *c*/*a* ratio is different from that of magnesium. The twin variant selection rule for primary and secondary twinning may thus be different. Based on such a consideration, a comprehensive examination of multiple twinning and its influence on crystallographic texture in a commercially obtained pure titanium sample (T40) has now been conducted. The material was deformed by multiple channel die compression (Paul *et al.*, 2012) and examined by the interrupted *in situ* SEM/EBSD (scanning electron microscopy/electron backscatter diffraction) orientation examination method (Bao, Lecomte *et al.*, 2010).

2. Experimental

The material used was a hot-rolled commercially pure titanium T40 sheet of dimensions 1000 × 1000 × 1.5 mm with the composition given in Table 1. The rolling direction is defined as RD, the transverse direction TD and the normal direction ND. Before deformation, the sheet was annealed at 1073 K for 2 h to allow the deformed microstructure to be fully recrystallized. The final average grain size was about 170 µm.

Samples of dimensions 15 × 10 × 1.5 mm were cut out, mechanically polished and further electrolytically polished at a temperature of 278 K in a solution of 100 ml of perchloric acid in 900 ml of methanol at 17 V (30 s) for subsequent SEM/EBSD measurements. On the polished surface, an area of 1250 × 950 µm was selected and marked by four micro-indentations. The microstructure and orientation maps of this selected area were measured by SEM/EBSD before and after each channel die compression step (reduction ratios of 0, 8, 16, 24 and 35%). The surface with the selected area was adhered firmly by a thin layer of cyanoacrylate super glue to another polished sample in a sandwich-like manner in order to maintain good surface quality. This is known as the split-sample technique. The channel die compression layout is illustrated in Fig. 1. In our channel die compression arrangement, the free elongation direction (FD in Fig. 1) is set to be parallel to the previous TD of the sheet, and the previous RD is blocked by the die. This blocked direction is denoted BD in the figure. The compression is applied in the previous ND. SEM/EBSD measurements were performed with a JEOL 6500F field-emission gun scanning electron microscope equipped with an EBSD acquisition camera at a step size of 0.6 µm at 15 kV. The data were acquired and processed with the *CHANNEL5* software (Oxford Instruments, Surrey, UK).

In order to obtain statistically significant results, 100 twinned grains were randomly selected for twin variant selection analyses. To eliminate the influence of grain size, only grains of a size between 150 and 200 µm were selected.

Table 1
Chemical composition of commercially pure titanium T40.

Element	H	C	N	O	Fe	Ti
Composition (p.p.m. by weight)	3	52	41	1062	237	Balance

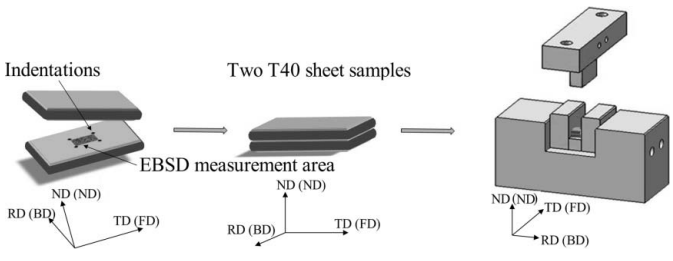

Figure 1
Schematic description of the channel die setup, where RD is the previous rolling direction, TD the transverse direction and ND the normal direction. For the present channel die compression, the free elongation direction (FD) is parallel to the previous TD, the die blocking direction (BD) is parallel to the previous RD and the compression is applied along the ND.

3. Results and discussion

3.1. Microstructure and texture

The orientation map of the initial sample shown in Fig. 2(*a*) reveals a completely recrystallized microstructure, in which the grains are coloured according to the orientation of each measured pixel. Fig. 2(*c*) presents the {0002} and {10$\bar{1}$0} pole figures (PFs) of the initial texture, studied in the Bunge coordinate setting (Bunge & Esling, 1981). The initial texture is characterized by two strong maxima at ±30°, tilted from the ND towards the TD in the {0002} PF, and by the maximum density of poles close to the RD in the {10$\bar{1}$0} PF, which is the typical texture observed in rolled Ti sheets (Lee *et al.*, 1988). This means that the majority of the grains have their *c* axes close to the ND, the load direction of the channel die compression. Clearly, the orientation of these grains is quite favourable to the {11$\bar{2}$2} compression (C) twin, as their *c* axes are close to the compression loading direction (Akhtar, 1975).

Fig. 2(*b*) exhibits the same area as shown in Fig. 2(*a*) after a reduction ratio of 8%. The boundaries of the {10$\bar{1}$2} tension twins (T1 twins) are marked in blue and those of the {11$\bar{2}$2} compression twins (C twins) in red. Two types of primary twin, the {10$\bar{1}$2} T1 twin and the {11$\bar{2}$2} C twin, and two types of double twin, a {10$\bar{1}$2} tension twin inside the {11$\bar{2}$2} compression twin (C-T1 double twin) and a {11$\bar{2}$2} compression twin inside the {10$\bar{1}$2} tension twin (T1-C double twin), are observed.

3.2. Theoretical misorientations of variants of double twins with respect to the matrix

In the literature (Partridge, 1967; Philippe *et al.*, 1988), three kinds of twins have been reported in deformed Ti at room temperature, *i.e.* the T1 and C twins observed in this work, plus another tension twin $\{11\bar{2}1\}$ (T2 twin) that has not been found in this work. Taking this additional T2 twin into account, six types of possible double twin could be expected in theory by combining any two of the three, namely C-T1 (a T1 tension twin formed inside a pre-existing C compression twin), T1-C, C-T2, T2-C, T1-T2 and T2-T1. As we know, six variants are possible for each type of twin system; therefore one double-twin combination could create 36 possible variants with respect to the initial matrix. Thus, the six sets of double-twin combinations create 216 possible variants in total. Conventionally, a twin variant is expressed with a minimum misorientation angle and a corresponding rotation axis with respect to the parent crystal. In addition to the minimum angle–axis expression, twin variants can also be distinguished in the form of pole figures. Both means of presentation are used in this study, as the information concerning the number and orientation of the variants with respect to the matrix provided by these two ways is complementary.

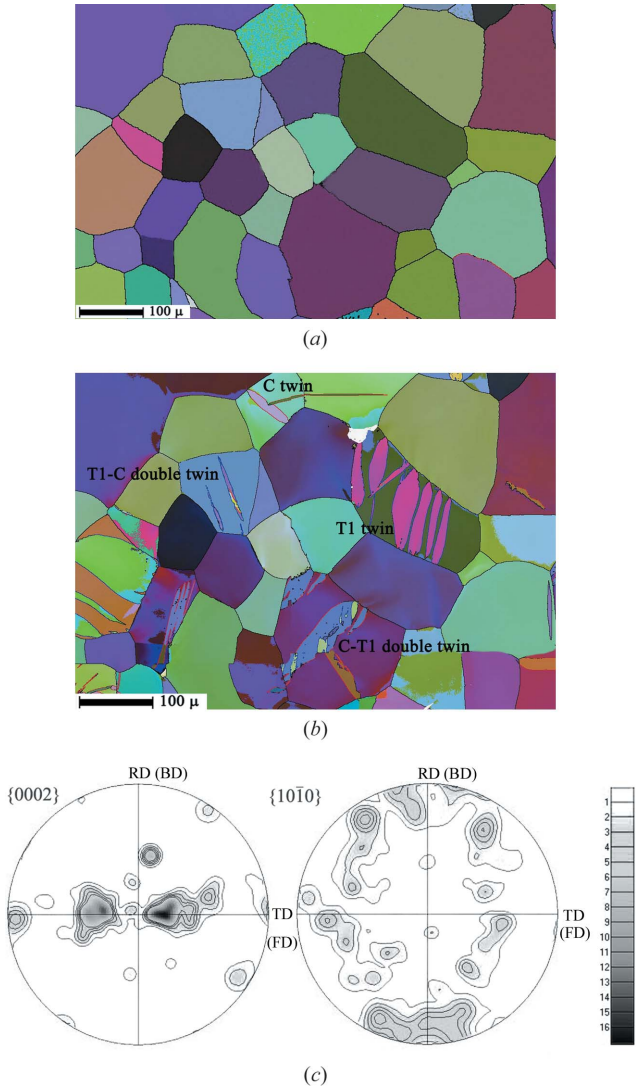

Figure 2
(*a*) Orientation map of the initial microstructure of T40 titanium. (*b*) Orientation map of the microstructure after a reduction ratio of 8%. Red lines represent $\{11\bar{2}2\}$ twin boundaries (C twin) and blue lines represent $\{10\bar{1}2\}$ twin boundaries (T1 twin). (*c*). The {0002} and $\{10\bar{1}0\}$ pole figures (PFs) of the initial texture. RD denotes the previous rolling direction, TD the previous transverse direction, FD the free elongation direction in the channel die compression and BD the die blocking direction.

Table 2
Data for various double twin combinations.

(*a*) Double twins combined with C and T1 twins (C-T1) or T1 and C twins (T1-C).

Group	Minimum angle–axis pair	Affected by twin order
A	41.3° $\langle 1\bar{5}43\rangle$	Yes
B	48.4° $\langle 5\bar{5}03\rangle$	No
C	87.9° $\langle 4\bar{7}30\rangle$	No

(*b*) Double twins combined with C and T2 twins (C-T2) or T2 and C twins (T2-C).

Group	Minimum angle–axis pair	Affected by twin order
D	29.5° $\langle 1\bar{1}00\rangle$	No
E	55.0° $\langle 5\,\bar{1}0\,5\,3\rangle$	No
F	80.6° $\langle 1\bar{1}00\rangle$	No
G	86.8° $\langle 5\,\bar{1}5\,10\,3\rangle$	Yes

(*c*) Double twins combined with T1 and T2 twins (T1-T2) or T2 and T1 twins (T2-T1).

Group	Minimum angle–axis pair	Affected by twin order
H	56.9° $\langle 4\,\bar{1}4\,10\,3\rangle$	Yes
I	66.5° $\langle 5\,\bar{1}5\,10\,3\rangle$	Yes
J	89.4° $\langle 4\,\bar{1}2\,8\,3\rangle$	Yes

The calculated misorientation of the variants is displayed in Table 2. The detailed calculation method is described by Cong *et al.* (2006). It is seen from Table 2 parts (*a*) and (*c*) that, for the C-T1 (or T1-C) and T1-T2 (or T2-T1) double twins, the six variants of each double twin can be divided into three classes according to their misorientation with respect to the matrix (groups *A*, *B* and *C* for C-T1 or T1-C, and groups *H*, *I* and *J* for T1-T2 or T2-T1), whereas for the C-T2 or T2-C double twins, the six variants can be divided into four classes (groups *D*, *E*, *F* and *G*). Therefore, the 216 variants can be classified into ten classes. We call these ten variant classes geometric variants in this paper. Obviously, variant differentiation by the minimum angle–axis criterion is neither sufficient nor precise. For example, we cannot see clearly if the final orientation of a double twin with respect to the matrix is affected by the order of the twins, *e.g.* C-T1 or T1-C. The pole figure representation is complementary to provide the missing information.

Fig. 3 displays the {0002} pole figures of all the calculated double-twin variants in the crystal basis of the matrix. In the figures, the matrix is represented by a star and primary twins by filled circles. The variants of the primary twins are distinguished by different colours. Double twins are represented by different symbols in different colours. Those resulting from the same primary-twin variant bear the same colour as their

primary-twin parent and the different symbols correspond to the minimum angle–axis group, as annotated in the key. Two variants belonging to one minimum angle–axis class, for example two variants in Group *A*, are named *A*1 and *A*2 and represented by a filled and an empty symbol, respectively.

It is seen clearly that the orientations of the variants in classes *A*, *G*, *H*, *I* and *J* (see Table 2) are affected by the twin order. For instance, although the double twins in the C-T1 and T1-C orders possess a misorientation angle of 41.3° about the $\langle 1\bar{5}43 \rangle$ axis, they bear two different rotations with respect to the orientation of the matrix. This surely induces different texture evolutions. Apparently, the orientation of the variants in classes *B*, *C*, *D*, *E* and *F* is not affected by the twin order. A further description concerning the effect of twin order is added in Table 2. Taking the twin-order effect into account, the ten variant classes can be further partitioned into 15 classes by extending the five minimum angle–axis classes affected by twin order into ten classes.

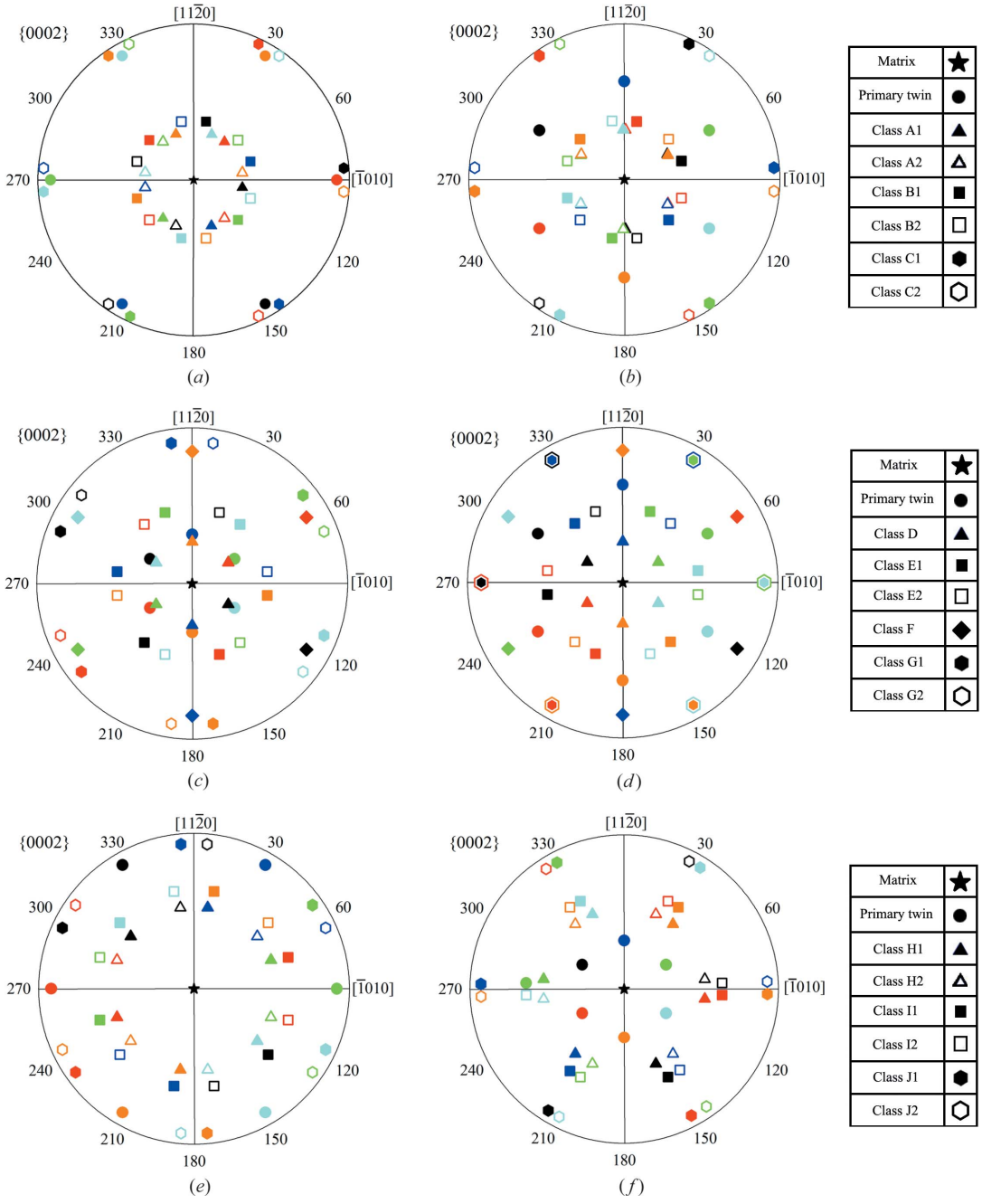

Figure 3
{0002} pole figures of all possible double twin variants. The matrix is represented as a star and the primary twins as filled circles. The variants of the primary twins are distinguished by different colours. Double twins are represented by different symbols in different colours. Those resulting from the same primary twin variant bear the same colour as the primary twin and the different symbols correspond to the minimum angle–axis group, as annotated in the key on each row. (*a*) The T1-C double twin. (*b*) The C-T1 double twin. (*c*) The T2-C double twin. (*d*) The C-T2 double twin. (*e*) The T1-T2 double twin. (*f*) The T2-T1 double twin.

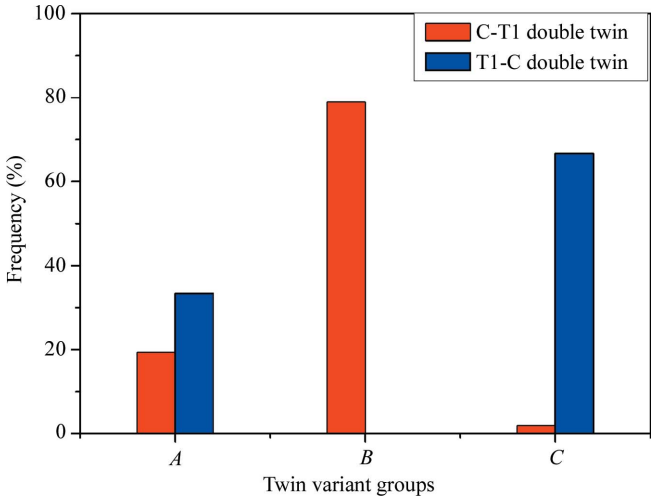

Figure 4
Frequency of occurrence of double twin variants in classes *A*, *B* and *C*.

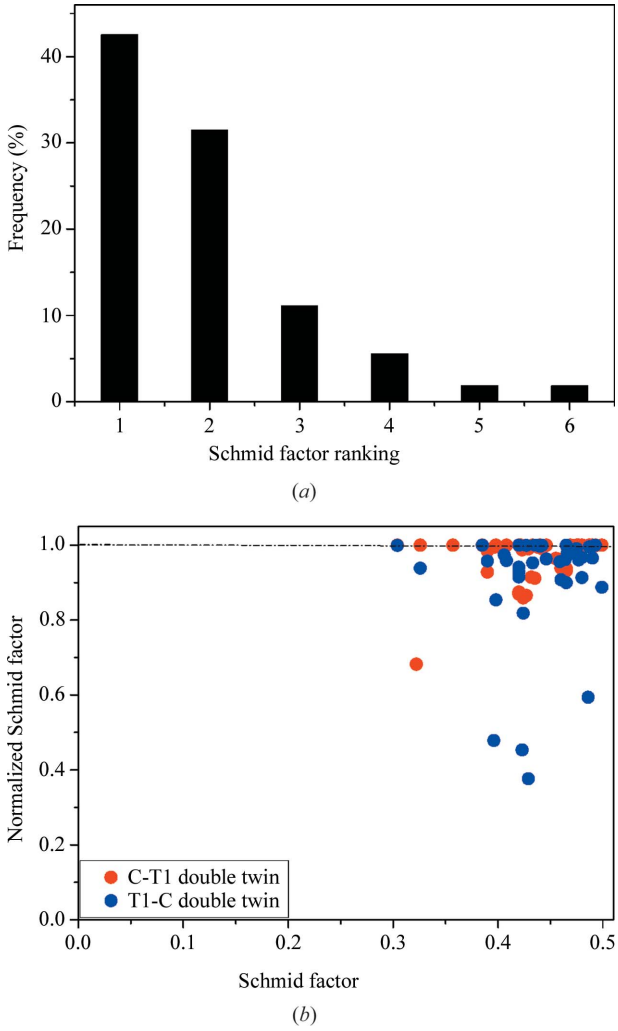

Figure 5
(*a*) Frequency of the active primary twin variants as a function of their SF rank with respect to the SF of the six possible variants (here, '1' is the highest and '6' the lowest). (*b*) SF normalized by the highest SF among the six possible variants (NSF) of the primary twins in C-T1 and T1-C double twins, as a function of their absolute SF.

Pole figures provide a clear schematic presentation of the evolution of orientation induced by double twinning. This information may be useful for theoretical simulations of texture evolution during plastic deformation of Ti alloys.

Owing to the absence of the T2 twin (the $\{11\bar{2}1\}$ tension twin) in the present study, the combination of C and T1 was the only case available to check possible variant selection of double twinning. With the purpose of performing a detailed and statistical analysis, 100 grains with double twins were studied one by one and C-T1 and T1-C double twins were analysed separately, despite the fact that the orientations of some of them are not affected by the two-pass order. The frequency of occurrence of each variant class in both C-T1 and T1-C double twins is presented in Fig. 4. It can be seen that class *B* (78.9% in frequency) dominates the other two in the C-T1 double twin. Class *A* occurs at 20% frequency and class *C* is nearly inactive (1.8%). In the case of the T1-C double twin, class *C* is predomint (66.7%) and class *A* occurs at 33.3% frequency. No variants from class *B* were found in the studied grains. The unusual proportions of class *C* in the C-T1 and class *B* in the T1-C double twin probably result from the relatively low SFs.

3.3. Variant selection of double twinning

3.3.1. Schmid factor analysis. The SF plays an important role in twin variant selection (Lebensohn & Tome, 1993). This study is the first to pay attention to the effect of the SF on variant selection in primary and secondary twinning. For each selected grain, the geometric SF was calculated in order to examine the resolved stress applied to the twinning system under the applied macroscopic compressive stress.

Primary twinning. The frequencies of the active primary twin variants ranked by SF corresponding to the six possible primary-twin variants were calculated and are shown in Fig. 5(*a*), where '1' is the highest and '6' is the lowest in SF ranking. It is seen that the majority of the active twin variants have a high SF ranking (about 43% for the first rank and 32% for the second rank). To understand further the role of the SF for the low-ranking variants, the normalized Schmid factor (NSF; Capolungo *et al.*, 2009) is adopted in the present work. In a given grain, the NSF of this grain equals the SF of the active variants (SF_a) divided by the highest SF (SF_h) of the six possible variants. If NSF = 1 then the active variant is the highest SF variant; if NSF < 1, a non-highest SF variant is activated instead of the highest SF one. The NSF is interesting in that it provides information about the extent to which the SFs of the active variants deviate from the highest SF in the case of an active variant with a non-highest SF. The NSF of the primary twin variants in the two double twins (C-T1 and T1-C) as a function of their absolute SF is displayed in Fig. 5(*b*). It can be seen that the NSF of most of the variants (C-T1 or T1-C) is higher than 0.85. This shows that, even if the SF rank of certain active variants is very low, their SFs are not really significantly different from the highest SF. From Fig. 5(*b*) one can see that nearly 90% of the active twins have an NSF higher than 0.85. This demonstrates that, in the present study, the

selection of primary twin variants is dominated by the SF. An NSF above 0.85 could thus be a useful indicator for predicting primary twin activation.

Secondary twinning. The SF ranking and the NSF of the secondary twins in the C-T1 and T1-C double twins were also examined. The frequency of the active secondary twins in both the C-T1 and T1-C double twins as a function of the SF ranking, and the NSF as a function of their absolute SF, are presented in Figs. 6(*a*) and 6(*b*), respectively. It is seen that, for the T1-C double twin, the activation of the majority of the variants is dominated by the macroscopic SF, whereas for the C-T1 double twin, although the majority of the active twins follow the SF law, the number of NSF variants decreases. This may be because C and T1 twins follow different growth mechanisms. A more detailed explanation can be found in our previous study (Bao *et al.*, 2011).

3.3.2. Geometric features of double-twin analysis. Fig. 7 shows the geometric configurations of the twinning elements [twin plane (TP), shear direction (SD) and shear plane (SP)] of the secondary twin variants in each class of the C-T1 and T1-C double twins with respect to the reference frame of the parent primary twinning elements, in the form of stereographic projections. In each variant class there are two distinct variants, represented by filled and empty symbols. Martin *et al.* (2010) suggested that, in magnesium, the growth potential of a secondary twin is strongly related to the angle of its shear plane normal direction (SPN) with that of the parent primary twin, and to the angle of its SD with that of the primary twin, because for primary twins the growth is mainly along the SPN and SD, especially along the SD, whereas for secondary twins the growth is limited by the lengths of the primary twin along these directions. Therefore, variants of double twins with small SPN and SD angles with respect to those of the primary twin should be favoured from the point of view of growth potential. In the case of titanium, the corresponding angles are summarized in Table 3. From the table, it is seen that, for both the C-T1 and T1-C double twins, class *B* possesses the most favourable conditions, or suffers the lowest limitation by the primary twins on the growth of secondary twins. Comparing this with the experimental observations in the present work (Fig. 4), one can see that class *B* in C-T1 double twins supports this argument well. It appears that 78.9% of the variants belong to class *B* in C-T1 double twins, prevailing over the other two classes. However, this hypothesis seems invalid in the case of T1-C double twins. Our experimental results (Fig. 4) exhibit a reverse result, and 66.7% of T1-C twin variants belong to class *C*, which has unfavourable conditions, whereas variants of class *B* are absent in the grains studied. Therefore, no consistent effect of geometric features is found on variant selection in double twins. This result indirectly validates the observation that the SF law is dominant in variant selection.

3.3.3. Effect of twinning on an adjacent grain. It is known that the twinning shear is along the twin direction on a succession of atomic layers parallel to the twinning plane.

Table 3
Geometric relations between the corresponding twinning elements of the secondary twins and those of their parent primary twins in each class.

(*a*) C-T1 double twins.

Variant group	Angle between primary and secondary twinning plane (TP)	Angle between primary and secondary twinning shear direction (SD)	Angle between primary and secondary SPN
A	84.1°	103.5°	30°
B	27.4°	23.7°	30°
C	66.9°	123.6°	90°

(*b*) T1-C double twins.

Variant group	Angle between primary and secondary twinning plane (TP)	Angle between primary and secondary twinning shear direction (SD)	Angle between primary and secondary SPN
A	84.1°	76.5°	30°
B	27.4°	23.6°	30°
C	66.9°	55.3°	90°

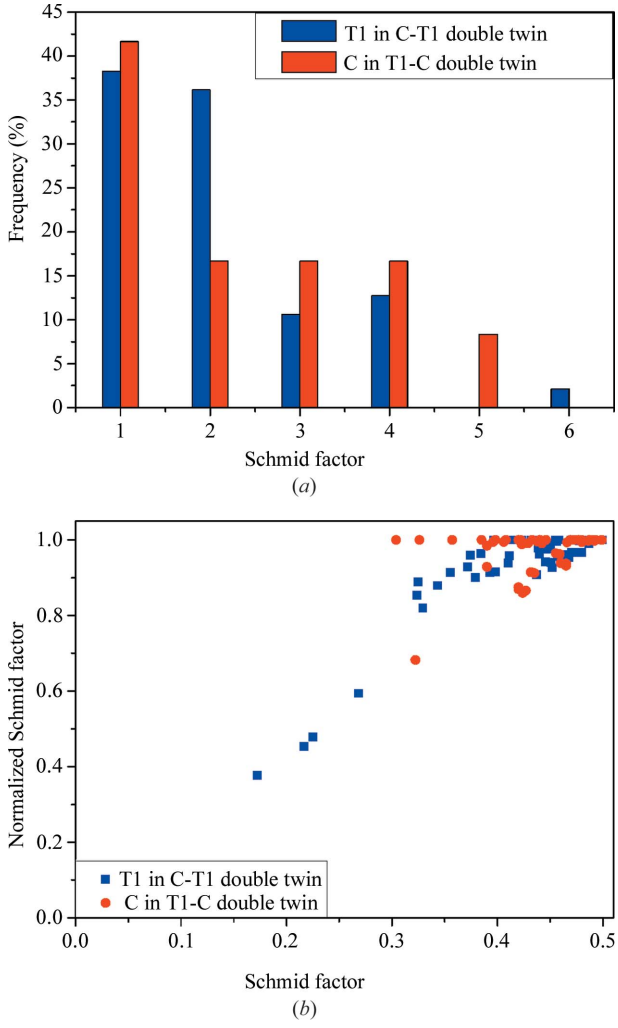

Figure 6
(*a*) Frequency of the active secondary twin variants as a function of their SF rank with respect to the SF of the six possible variants (here, '1' is the highest and '6' the lowest). (*b*) SF normalized by the highest SF among the six possible variants (NSF) of the secondary twin variants in C-T1 and T1-C double twins, as a function of their absolute SF.

Once the twinning shear encounters an obstacle (grain boundary, twin boundary or phase boundary), it will be either diverted or blocked by the obstacle. This inevitably leads to the accumulation of lattice distortion at the front of the obstacle, and the formation of a local and boundary-centred high-energy region that may induce the activation of a new twin in an adjacent grain (Yoo, 1969). On orientation maps, this appears as if the twins have sheared across grain boundaries and continued into adjacent grains. In our observation, however, the more common case is that twins are blocked at the boundaries. For those that crossed boundaries, we conducted an examination of the occurrence frequency of such through-boundary twins as a function of the angle between adjacent twinning planes on both sides of the obstacle boundary. The results are shown in Fig. 8. It can be seen that, for most of the through-boundary twins, the deviation of a twinning plane from an adjacent twinning plane on the other side of the obstacle boundary is less than 20°. For those that terminate at the obstacle boundary, this angle is usually much higher.

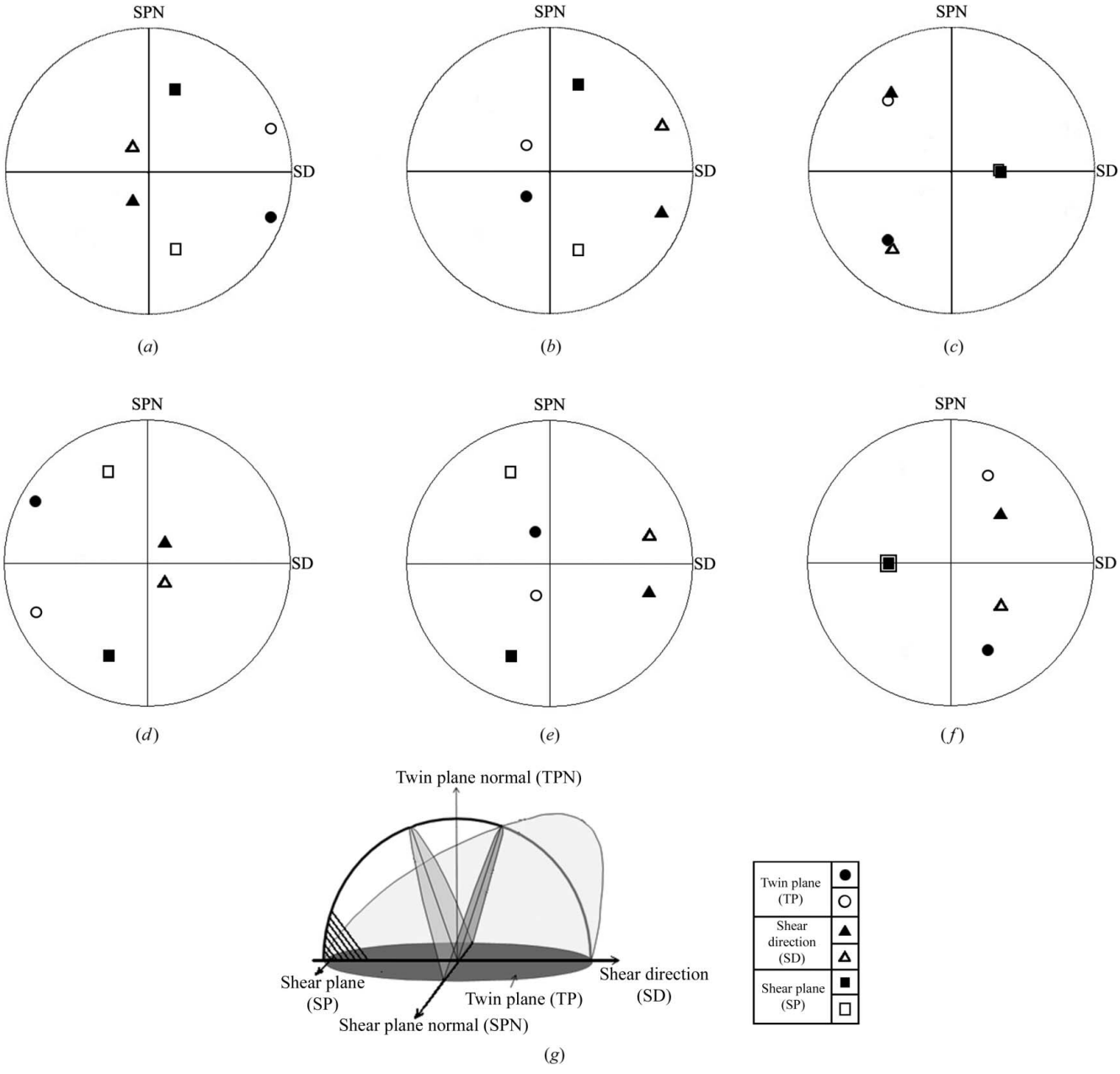

Figure 7
Stereographic projections of the twinning plane (TP), the shear direction (SD) and the shear plane (SP) of the secondary twin variants in classes *A*, *B* and *C* of the C-T1 and T1-C double twins in the reference frame of the twinning elements [shear direction (SD), shear plane normal (SPN) and twinning plane normal (TPN)] of their parent primary twin. (*a*) Class *A* in C-T1 double twin. (*b*) Class *B* in C-T1 double twin. (*c*) Class *C* in C-T1 double twin. (*d*) Class *A* in T1-C double twin. (*e*) Class *B* in T1-C double twin. (*f*) Class *C* in T1-C double twin. (*g*) Diagram illustrating definitions used.

3.4. Evolution of misorientation distribution and texture

The misorientation angle distribution provides misorientation information between each pixel and its neighbouring pixels in orientation maps. This analysis has been used in the present work to obtain the amount of different types of twinning. In order to eliminate small-angle misorientation caused by dislocations, only angles larger than 10° are included in the present analysis. The misorientation angle distributions of the initial state and the 16 and 35% reduction ratios are shown in Fig. 9. It is seen that, at a reduction ratio of 16% (Fig. 9*b*), three characteristic peaks appear in the spectrum: a peak at 65°, which is the highest and corresponds to the primary C twin, a peak at 85°, which is the second highest and corresponds to the primary T1 twin, and a small peak at 88°, which corresponds to the group *C* double twin. This suggests that C twinning is dominant for this deformation state. This result is reasonable considering that the initial texture favours the occurrence of a C twin. The weak peak around 88°, which corresponds to the group *C* double twin, demonstrates that double twinning starts at this state (16%). When the reduction ratio increases to 35% (Fig. 9*c*), the frequency of the C twin decreases markedly and three other peaks at 41, 48 and 88°, corresponding to the three variant classes (*A*, *B* and *C*) of C-T1 or T1-C double twins, evidently increase. It is also seen from Fig. 9(*c*) that at 35% deformation the frequency of the variants in class *C* is about twice that of classes *A* or *B*, and no obvious difference in frequency is observed between classes *A* and *B*.

The texture evolution is presented in Fig. 10 as a set of {0002} and {10$\bar{1}$0} PFs at reduction ratios of 0 (initial), 8, 16, 24 and 35%. It is seen that texture evolution is characterized by a shift of the two strong maxima from the TD towards the RD in the {0002} PF. The maximum intensity level decreases from 16 in the initial state (Fig. 10*a*) to nine at 35% reduction (Fig. 10*e*). From the texture evolution presented in Fig. 10, one can deduce that the channel die deformation used in the present work has a close similarity to rolling. Similar to rolling, channel die deformation allows only one free elongation direction of the deformed metal; the transverse direction is blocked by the die. In our channel die compression arrange-

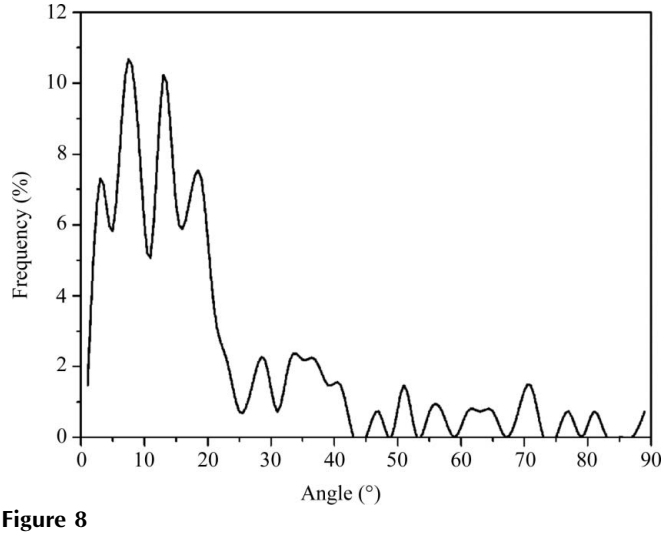

Figure 8
Frequency of the active through-boundary twin variants as a function of the angle between their twinning planes on both sides of the boundary.

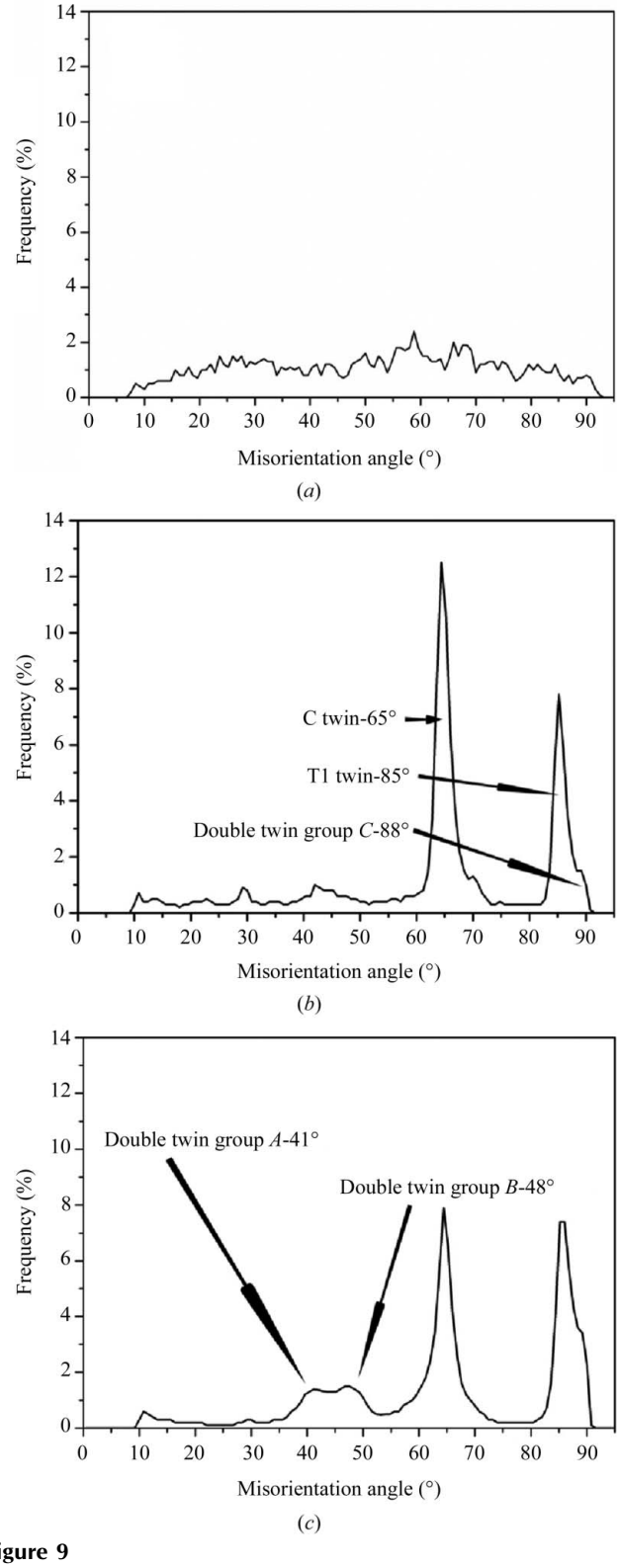

Figure 9
Misorientation angle distribution of (*a*) the initial sample, and after reduction ratios of (*b*) 16% and (*c*) 35%.

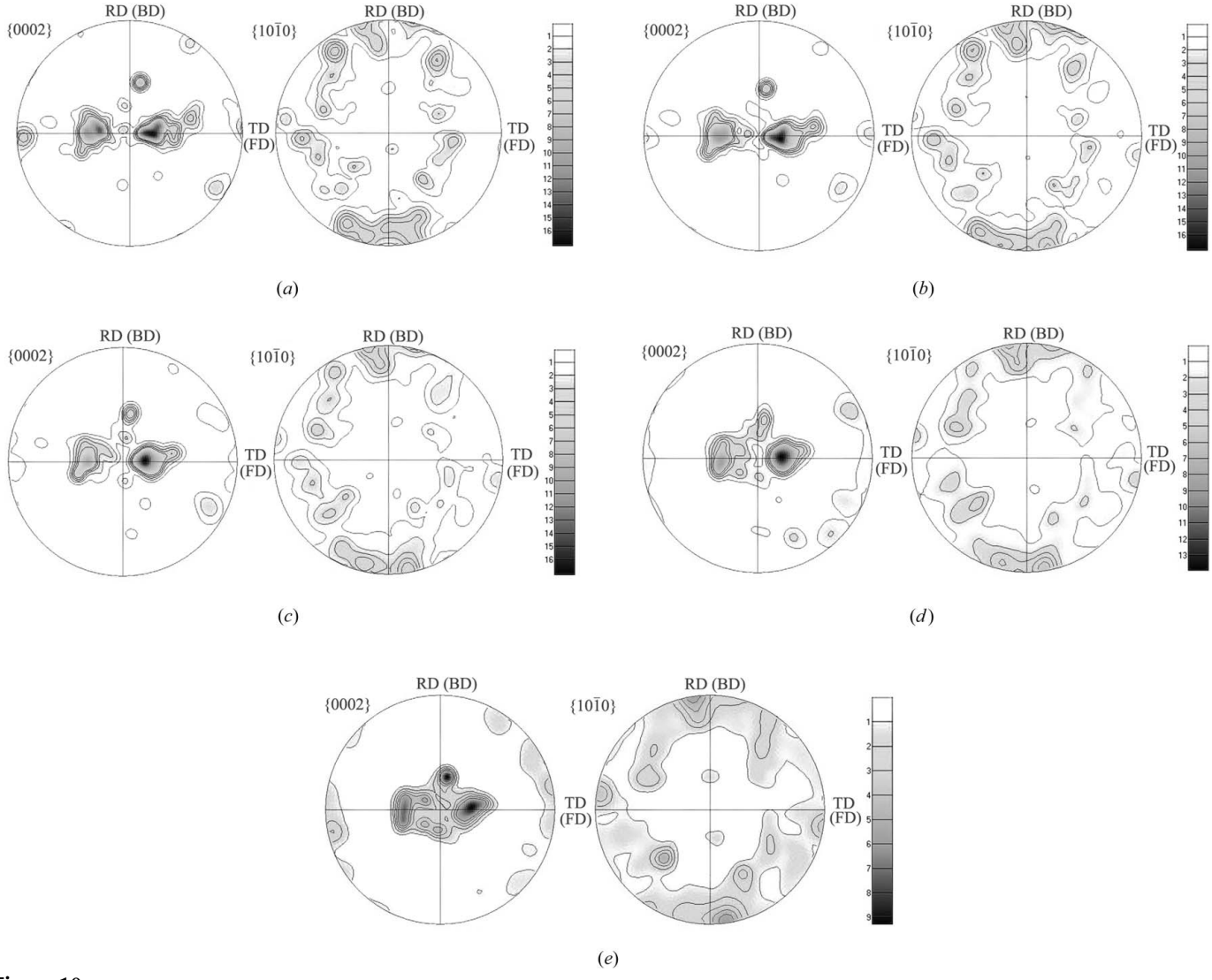

Figure 10
{0002} and {10$\bar{1}$0} pole figures measured at reduction ratios of (*a*) 0% (initial sample), (*b*) 8%, (*c*) 16%, (*d*) 24% and (*e*) 35%, where RD is the previous rolling direction, TD the previous transverse direction, FD the free elongation direction in the channel die compression and BD the die blocking direction.

ment, the free direction corresponds to the previous TD and the blocked direction corresponds to the previous RD. The texture thus evolves into new stable orientations by shifting the two maxima towards the previous RD. Clearly, twinning provides significant contributions to this texture evolution (Chun *et al.*, 2005; Bao, Schuman *et al.*, 2010). The weakening of texture intensity during deformation in the present work is also due to twinning. By forming twin variants, one initial orientation is split into several new orientations, as illustrated in Fig. 3. As the initial texture of the present material is favourable for twinning, the initial orientations give rise to many new orientations through primary and secondary twinning, thus leading to weakening of the global texture intensity.

4. Conclusion

In this study, an investigation of various factors on twin variant selection in multiple twins in channel die compressed titanium T40 was performed. The main conclusions can be summarized as follows:

(*a*) Twinning order does affect the resulting orientation induced by multiple twinning, even though the double twins are identical in misorientation angle and axis representation. All the double twin variants can be partitioned into 15 orientation variant classes in terms of their final orientation with respect to the orientation of the matrix, rather than ten geometric variant classes in terms of their minimum misorientation angle–axis.

(*b*) Strong variant selection takes place in C-T1 and T1-C multiple twins. Group *B* (78.9%) dominates over the other two in the C-T1 multiple twin, whereas class *C* (66.7%) dominates over the other classes in T1-C double twins.

(*c*) Schmid factor analysis is performed on both the primary twin and the secondary twin variants. The SF gives an accuracy of about 45% for predicting the primary twin variant selection and 40% for the secondary twin variant selection. It is

suggested that, if the NSF were to be adopted in addition to the classical Schmid law in predicting the selected variant, the accuracy would rise to 90%. No consistent influence of geometric features is found on variant selection in double twins.

(*d*) The twins formed in one grain may induce a new twin in an adjacent grain, provided that the angle between the two twinning planes from the two grains is smaller than 20°.

(*e*) Twinning affects texture evolution by reorienting the previous stable orientation into a new orientation. Through splitting the orientations by forming new orientations through multiple twinning, the global texture is weakened.

This study was supported by the Federation of Research for Aeronautics and Space (Fédération de Recherche pour l'Aéronautique et l'Espace Thème Matériaux pour l'Aéronautique et l'Espace), by the project OPTIMIST (Optimisation de la mise en forme d'alliages de titane), by the Chinese Postdoctoral Science Foundation (grant No. 2012M520634) and by the Fundamental Research Funds for the Central Universities (grant No. N120309003).

References

Akhtar, A. (1975). *Metall. Mater. Trans. A*, **6**, 1105–1113.
Balogh, L., Tichy, G. & Ungár, T. (2009). *J. Appl. Cryst.* **42**, 580–591.
Bao, L., Lecomte, J. S., Schuman, C., Philippe, M. J., Zhao, X. & Esling, C. (2010). *Adv. Eng. Mater.* **12**, 1053–1059.
Bao, L., Schuman, C., Lecomte, J. S., Philippe, M. J., Zhao, X. & Esling, C. (2011). *Adv. Eng. Mater.* **13**, 928–932.
Bao, L., Schuman, C., Lecomte, J. S., Philippe, M. J., Zhao, X., Zuo, L. & Esling, C. (2010). *Comput. Mater. Continua*, **394**, 1–15.
Barnett, M., Keshavarz, Z., Beer, A. & Ma, X. (2008). *Acta Mater.* **56**, 5–15.
Bevis, M. & Tomsett, D. I. (1970). *J. Appl. Cryst.* **3**, 342–348.
Bunge, H. J. & Esling, C. (1981). *J. Appl. Cryst.* **14**, 253–255.
Capolungo, L., Marshall, P. E., McCabe, R. J., Beyerlein, I. J. & Tomé, C. N. (2009). *Acta Mater.* **57**, 6047–6056.
Chateigner, D., Camana, G. & Trimby, P. (2002). *Mater. Sci. Forum*, **408–4**, 1675–1679.
Cheneau-Späth, N., Fillit, R. Y. & Driver, J. H. (1994). *J. Appl. Cryst.* **27**, 980–987.
Chun, Y. B., Yu, S. H., Semiatin, S. L. & Hwang, S. K. (2005). *Mater. Sci. Eng. A*, **398**, 209–219.
Cong, D. Y., Zhang, Y. D., Wang, Y. D., Esling, C., Zhao, X. & Zuo, L. (2006). *J. Appl. Cryst.* **39**, 723–727.
Fundenberger, J. J., Philippe, M. J., Wagner, F. & Esling, C. (1997). *Acta Mater.* **45**, 4041–4155.
Godet, S., Jiang, L., Luo, A. A. & Jonas, J. J. (2006). *Acta Mater.* **55**, 1055–1058.
Jonas, J. J., Mu, S., Al-Samman, T., Gottstein, G., Jiang, L. & Martin, E. (2011). *Acta Mater.* **59**, 2046–2056.
Kocks, U. F. & Westlake, D. G. (1967). *Trans. Metall. Soc. AIME*, **239**, 1107–1109.
Lebensohn, R. A. & Tome, C. N. (1993). *Philos. Mag. A*, **67**, 187–206.
Lee, H. P., Esling, C. & Bunge, H. J. (1988). *Texture Microstruct.* **7**, 317–337.
Mahajan, S. & Williams, D. F. (1973). *Int. Mater. Rev.* **18**, 43–61.
Martin, E., Capolungo, L., Jiang, L. & Jonas, J. J. (2010). *Acta Mater.* **58**, 3970–3983.
Mu, S., Jonas, J. & Gottstein, G. (2012). *Acta Mater.* **60**, 2043–2053.
Nespolo, M. (2004). *Z. Kristallogr.* **219**, 57–71.
Nespolo, M. & Ferraris, G. (2000). *Z. Kristallogr.* **215**, 77–81.
Nespolo, M. & Ferraris, G. (2003). *Z. Kristallogr.* **218**, 178–181.
Nespolo, M. & Ferraris, G. (2004). *Acta Cryst.* A**60**, 89–95.
Nespolo, M. & Ferraris, G. (2006). *Acta Cryst.* A**62**, 336–349.
Partridge, P. G. (1967). *Int. Mater. Rev.* **12**, 169–194.
Paul, H., Morawiec, A. & Baudin, T. (2012). *Metall. Mater. Trans. A*, **43**, 4777–4793.
Philippe, M. J., Esling, C. & Hocheid, B. (1988). *Texture Microstruct.* **7**, 265–301.
Philippe, M. J., Serghat, M., Van Houtte, P. & Esling, C. (1995). *Acta Metall. Mater.* **43**, 1619–1630.
Rosi, F. D., Perkins, F. C. & Seigle, S. S. (1956). *J. Metals*, **8**, 115–122.
Vedoya, P., Pochettino, A. & Penelle, R. (1988). *Texture Microstruct.* **8**, 601–610.
Yoo, M. H. (1969). *Trans. Metall. Soc. AIME*, **245**, 2051–2060.
Yoo, M. H. (1981). *Metall. Mater. Trans. A*, **12**, 409–418.
Zaefferer, S. (2003). *Mater. Sci. Eng. A*, **344**, 20–30.
Zhang, Y., Li, Z., Esling, C., Muller, J., Zhao, X. & Zuo, L. (2010). *J. Appl. Cryst.* **43**, 1426–1430.